Additive Manufacturing 79 (2024) 103945

Contents lists available at ScienceDirect

Additive Manufacturing

journal homepage: www.elsevier.com/locate/addma

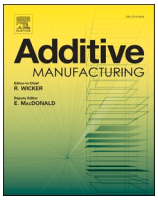

Additive manufacturing of functionally graded foams: Material extrusion process design, part design, and mechanical testing

Karun Kalia, Amir Ameli *

Department of Plastics Engineering, University of Massachusetts Lowell, 1 University Ave, Lowell, MA 01854, USA

ARTICLE INFO

Keywords:
Functionally graded foam
Cellular plastic
Material extrusion additive manufacturing
Thermally expandable microsphere

ABSTRACT

Functionally graded foams (FGFs) were in-situ fabricated via material extrusion (MEX) additive manufacturing (AM) process. Foamable filaments loaded with thermally expandable microspheres (TEMs) at 8.0 wt% was first fabricated using a single screw extruder. The correlations between the resultant foam density and process factors, namely nozzle temperature (NT) and flow rate (FR) were established using a statistical analysis and the density predictability of the model was verified by experiment. With concurrent control of NT and FR, FGFs with density ranges as high as 0.86 g cm^{-3} were achieved within a single print. Various FGFs were designed using linear, concave, and convex density gradient functions. The density-process correlation model was then used to obtain the NT and FR parameters needed to produce the density values as demanded by the part design. FGFs along with their single density foam (SDF) counterparts were successfully printed with good dimensional stability. Under quasi-static compression testing, all FGFs showed higher energy absorption capacity at low stress levels, as compared to their SDF counterparts. Moreover, under impact conditions, a significant loading direction dependency was found for the FGFs. Overall, this work demonstrates the AM feasibility of FGFs as a single print with tailored density profiles which can be used in generative design optimization of AM parts for enhanced mechanical performance and other functionalities.

1. Introduction

The demand of lightweight and customizable materials for a variety of applications in high shock absorbance, thermal insulation, damping, and packaging has led to the development of cellular foam 3D printing technologies integrated with material extrusion (MEX) additive manufacturing (AM) process [1,2]. Impregnation of filament with CO_2 gas [3–7], use of chemical blowing agent [8,9], and incorporation of thermally expandable microspheres (TEMs) in the filament are some ways to realize the cellular structures in thermoplastics during MEX AM process [10–13]. There are also some reports in which proprietary foamable filaments were used [14,15] whereas, some have utilized dual nozzle printing process in which secondary nozzle was used to dispense the foam into thin walled structures [16–18]. The successful coupling of foaming and MEX AM processes within a single process may provide an opportunity to print functionally graded foams (FGFs).

FGFs are engineered with controlled porosity distribution and graded density structure which allows enhancement in energy absorption capacity, efficient use of material, and tailored engineering design for applications such as helmet pads, knee pads, tissue restorative scaffolds, etc. [19]. There have been several numerical [20,21] and experimental reports [22–25] on understanding the mechanical behavior of FGFs. Gupta et al. [22] reported that the density graded syntactic foams provide higher absorption energy as compared to single density syntactic foams. Apart from that, literature also discusses the effect of the density gradient orientation, i.e., high-to-low or low-to-high density variation with respect to the applied force direction on the quasi-static compressive and dynamic impact behavior of graded foams [26]. The slope of density gradient, i.e., the rate of change in the density with respect to the sample dimension in the loading direction (height) has also been shown to have an effect on the energy absorption capability of the foams as compared to their baseline single-density parts [21].

Fabrication of FGFs using traditional manufacturing processes is a challenging process, especially for complex part geometries. FGFs are usually made by adhesively bonding several discrete layers having various densities [27,28], which requires additional post-processing and encounters debonding issues during service. The fabrication of FGFs have also been reported using batch foaming [29], extrusion foaming [30,31], foam injection molding [32–34], and particulate leaching [35] processes. However, the control of density gradient in these processes is

* Corresponding author.
E-mail address: Amir_Ameli@uml.edu (A. Ameli).

https://doi.org/10.1016/j.addma.2023.103945
Received 7 September 2023; Received in revised form 27 November 2023; Accepted 21 December 2023
Available online 24 December 2023

Nomenclature

PLA	Polylactic acid
TEM	Thermally expandable microspheres
MEX AM	Material extrusion additive manufacturing
SEM	scanning electron microscope
FGF	Functionally graded foam
SDF	Single density foam
ρ	Density (g cm^{-3})
$\Delta\rho$	Density range (g cm^{-3})
N	Cell density (cells cm^{-3})
n	Total number of cells
A	Microstructure cross-sectional area (cm^2)
h_i	Height of section i of foam
H	Total height of foam
m	Density gradient exponent
FR	Flow rate
NT	Nozzle temperature
C-FR	Coded value of flow rate
C-NT	Coded value of nozzle temperature
C-NT × FR	Coded value of interaction between nozzle temperature and flow rate
SD	Standard deviation
ANOVA	Analysis of variance
R^2	Coefficient of determination of regression model
LIN	Linear density gradient
CVX	Convex density gradient
CNV	Concave density gradient
L-H_LIN	FGF with linear (LIN) low to high (L-H) density gradient in applied force direction
H-L_LIN	FGF with linear (LIN) high to low (H-L) density gradient in applied force direction
L-H_CVX	FGF with convex (CVX) low to high (L-H) density gradient in applied force direction
H-L_CVX	FGF with convex (CVX) high to low (H-L) density gradient in applied force direction
L-H_CNV	FGF with concave (CNV) low to high (L-H) density gradient in applied force direction
H-L_CNV	FGF with concave (CNV) high to low (H-L) density gradient in applied force direction

difficult and these processes do not lend themselves easily for the fabrication of FGFs that may need complex density variations based on the part design criteria.

Coupling MEX AM and in-situ foaming processes towards manufacturing of FGFs offers several benefits. The followings are the advantages of MEX AM that may be beneficial in the manufacturing of FGFs: a) foamed parts can be made with partial infill which further lowers the bulk density, b) feasibility of printing complex geometries, and c) layer-wise manufacturing wherein the density of each layer may be controlled. Some authors have shown the feasibility of graded structures using lattices and by controlling the infill density in MEX AM parts [36]. This approach is however limited by the raster resolution and density ranges. Moreover, it cannot provide a cellular structure within each raster. In-situ foaming within MEX AM process may provide a potential solution to the manufacturing of functionally graded structures using true microcellular morphology. It is worth noting that in-situ foaming can also be integrated with lattice structure design, where each one provides lightweighting strategy at different scales. In-situ foaming via MEX AM process offers several advantages such as low material usage, ease of microstructure control, mitigation of shrinkage and inter-bead voids in 3D-printed parts, and additional design freedom [10–12,37]. Previously, the authors have demonstrated the successful filament fabrication and the feasibility of printing foams with highly uniform cellular morphologies and dimensional stability [12,38] and established the process-structure-property relationships in 3D printed microcellular foams enabled by the incorporation of TEMs [13]. Recently, Ozdemir et al. have demonstrated that the translucency, gloss, and texture of the printed parts via MEX AM can be controlled by inducing various degrees of foaming during printing [39].

Table 1
Print process parameters utilized for printing FGFs and SDFs.

Variable parameters	
Nozzle temperature (°C)	154-220 °C
Flow rate (%)	15-86 %
Fixed parameters	
Nozzle diameter (mm)	0.8
Raster width (mm)	0.8
Layer height (mm)	0.3
Bed temperature (°C)	55
Print speed (mm.s^{-1})	25
Filling pattern (°)	lines (0 °)
Infill density (%)	100

The objective of this study was to establish a microcellular foaming platform within MEX AM through which any FGFs with density gradient in the height direction can be designed and fabricated through only process control using only one filament on a commercially available MEX 3D printer. The framework includes the approaches to model the process-density correlation, design of FGFs with various density gradients, 3D printing and density verification, as well as mechanical performance evaluations. To this end, polylactic acid (PLA) feedstock filament loaded with 8.0 wt% TEM was first fabricated with excellent dispersion using a single screw extruder having special mixing sections and utilized as the feedstock for MEX AM of foams. During the MEX AM process, nozzle temperature, flow rate, and their various combinations were assessed with a goal of achieving a relatively wide range of density in the printed foams. The density and the microcellular structure of the printed foams were thoroughly discussed in relation to the process variables. A density-process correlation statistical model was developed, experimentally verified, and then utilized to generate flow rate and nozzle temperature parameters required to print any desired density within the FGF structures. FGFs were then designed with linear, concave, and convex density profiles. The FGFs and their single density foam (SDF) counterpart, having an equivalent overall density, were then 3D printed and tested for their mechanical performance under quasi-static compression and low-velocity drop impact loading and the differences between various FGFs and SDFs were discussed.

2. Materials and methods

2.1. Materials and filament fabrication process

NatureWorks PLA Ingeo 4043D grade and foaming agent Sekisui advancell EM501E1 (TEM) at 8.0 wt% were dry mixed and fed into a Dr Collin E30P single screw extruder (L/D of 25) to fabricate the foamble filament of PLA. EM501E1 is a master-batch with 50 wt% TEM and 50 wt% polyethylene carrier phase and has an intital particle size of 21–31 μm and overall density of 1.24 g cm^{-3}. The extruder barrel zone temperatures Z1, Z2, Z3, Z4 and Z5 were set at 145, 151, 151, 147 and 125 °C, respectively at a screw speed of 4 rpm. The melt temperature near the die and the die pressure obtained were 145 ± 2 °C and 65 ± 3 bar, respectively. PLA/TEM8.0 % filament was passed through a water bath and collected using a filabot spooler at a controlled diameter of 1.65 ± 0.03 mm. Measured density of the filament was 1.12 ± 0.02 g. cm^{-3} which is only about 10 % lower than the density of neat PLA Ingeo

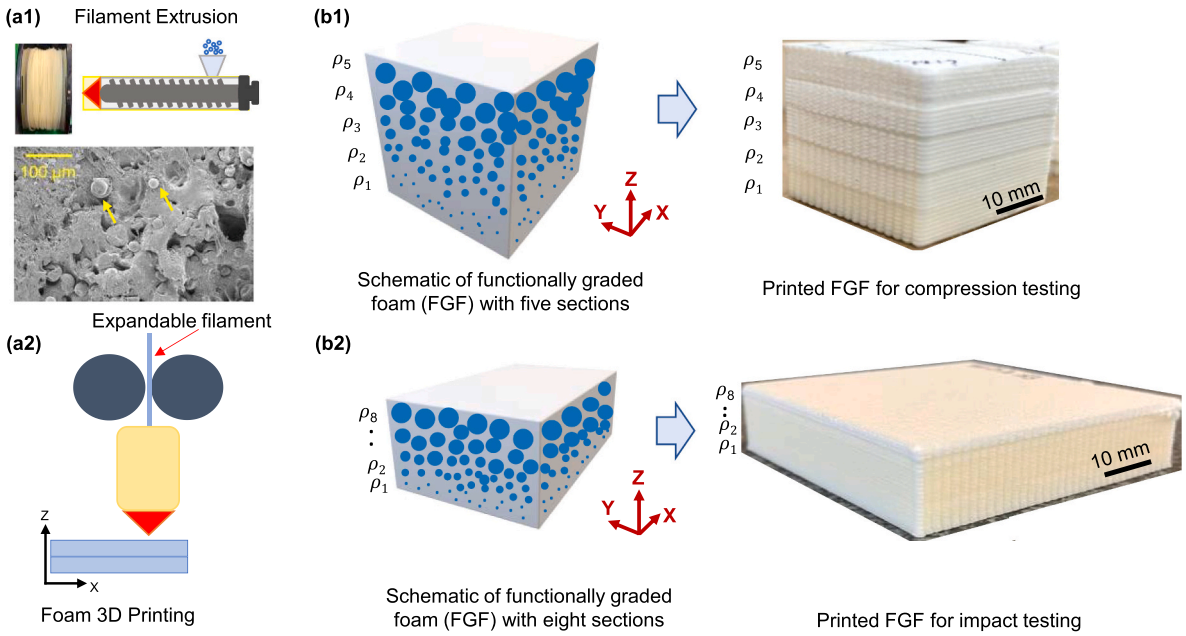

Fig. 1. Illustration of the filament extrusion and in-situ foam 3D printing processes. (a1) shows the extrusion process with a spool of expandable filament and a SEM micrograph of filament cross-section revealing unexpanded TEMs. (a2) provides a simple schematic of the foam MEX AM. (b1) and (b2) show the schematic illustration and actual printed FGFs with two different dimensions used for compression test and drop impact test, respectively. The cellular morphology and density vary along the Z direction. ρ_1 is the highest density and the density decreases as Z increases.

4043D indicating that the foaming during filament fabrication process was successfully suppresed. More details on the filament fabrication process can be found elsewhere [12,38].

2.2. Material extrusion additive manufacturing process (MEX AM)

Foamable PLA/TEM8.0 % filament was fed into a commercially available Raise 3D Pro2 printer. Ideamaker slicing software was used to slice the SolidWorks file and assign corresponding print process

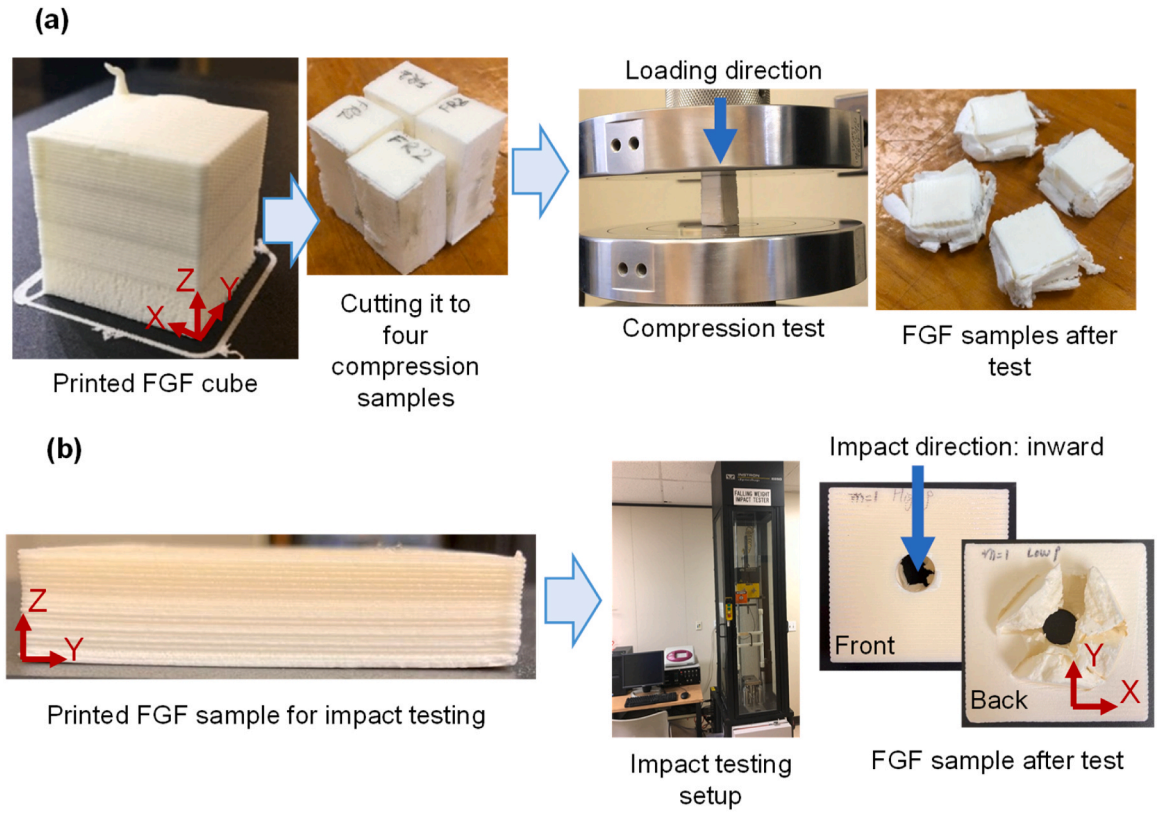

Fig. 2. Illustration of (a) the FGF prints, before and after cutting to four samples, loaded under compression setup, and after the compression test is complete, and (b) the printed FGF impact samples before testing, loaded under drop weight impact testing, and after the test is complete.

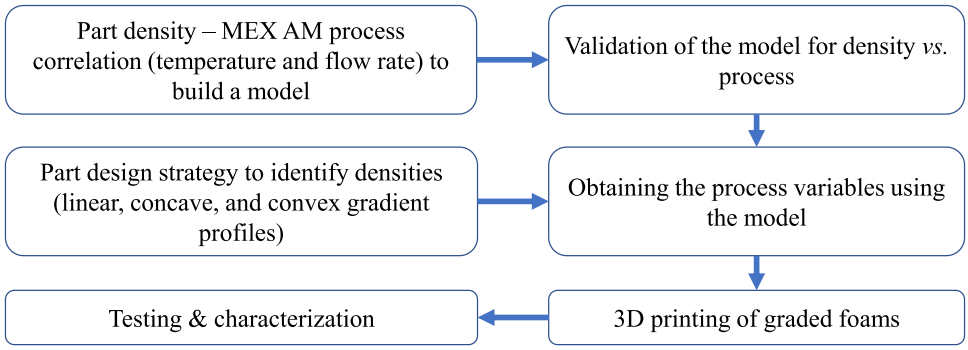

Fig. 3. Flow diagram showing the steps in the establishment of MEX AM process to manufacture FGFs: Density-process correlation and part design were used together to identify the required density in each section of FGFs as well as the process factor levels that produced the same density. The parts were then 3D printed and tested.

parameters and print paths to each section of the part. Table 1 represents the variable and fixed print process parameters utilized in printing FGFs and SDFs. Nozzle temperature and flow rate parameters were varied and their effects on the evolved microstructure and the bulk density were studied. The remaining printing parameters were kept unchanged as listed in Table 1.

Fig. 1(a1-a2) schematically illustrates the filament extrusion and printing processes and Fig. 1(b1-b2) shows the schematics and actual samples of FGF structures with five and eight sections, respectively, each section having a particular density (ρ) where ρ_1 is the highest bulk density section and has the smallest TEM cell size and/or the least number of activated TEMs, thereby yielding a lower degree of foaming. With an increase in the height along Z direction, the process parameters are changed such that the TEM cell size and/or the number of activated TEMs increase, causing a further decrease in the density, reaching to the lowest density, i.e., ρ_5 or ρ_8 sections of Fig. 1(b1) or (b2), respectively. With such change in the cellular morphologies along the Z direction, a gradient of bulk density is achieved. The samples shown in Fig. 1(b1) and (b2) were used for quasi-static compression test and drop impact test, respectively.

2.3. Characterizations

2.3.1. Density and electron microscopy

ASTM D792 standard was followed to measure the densities of the parts using Mettler Toledo MS303TS/ 00 density kit. JEOL JSM 6390 scanning electron microscope (SEM) was used to observe the morphologies at the cross-sections of printed foams under an acceleration voltage of 5 kV. Prior to SEM, samples were cryo-fractured, and Au sputter coated using Denton vacuum sputter coater for 6 min at currents between 3–4 mA.

2.3.2. Cell density and cell size

SEM images at magnification of 50 taken in Y-Z plane (Fig. 1) were used to analyze the cellular morphologies and calculate the cell density and cell size of the printed foams. ImageJ, an open-source software was used for image processing. Cell density N (cells.cm^{-3}) was measured using equation:

$$N = \left(\frac{n}{A}\right)^{3/2} \quad (1)$$

where n is the total number of cells and A is the cross-sectional area in cm^2. The mean and standard deviation of cell density and cell size were calculated using at least three SEM images taken from three sample replicates.

2.3.3. Mechanical testing

Fig. 2(a) and (b) show the quasi-static compression test and drop weight impact test, respectively. Quasi-static compression testing and low-velocity impact testing were conducted to study the performance of the FGFs as well as their SDF counterparts. Quasi-static compression samples were made with dimensions of L × W × H as 27 × 27 × 24 mm^3, which were then cut down to four cuboids shaped FGFs using a band saw cutter machine to the final sample dimensions of 13.5 × 13.5 × 24 mm^3. Testing was conducted using an Instron 5966 load frame with load cell capacity of 10 kN at a speed of 10 mm min^{-1}. FGFs were tested by orienting the maximum density side to be in contact with the moving platen. For low-velocity impact testing, FGFs and their SDFs counterparts were tested as per ASTM D3763 standard, and the sample dimensions were L × W × H of 55 × 55 × 12 mm^3. Instron 8250 falling

Table 2
All the examined nozzle temperature (NT) and flow rate (FR) combinations along with the measured density of each segment, its standard deviation (SD), and coefficient of variation (COV).

Part Section	NT-actual (°C)	NT-coded (dimensionless)	FR-actual (%)	FR-coded (dimensionless)	ρ (g cm^{-3})	SD (g cm^{-3})	COV (%)
Block 1: Density vs. nozzle temperature							
I	185	-0.06	35	-0.436	0.389	0.015	3.856
II	195	0.242	35	-0.436	0.345	0.022	6.376
III	205	0.545	35	-0.436	0.290	0.020	6.896
IV	215	0.848	35	-0.436	0.263	0.013	4.942
Block 2: Density vs. flow rate							
I	200	0.393	15	-1.000	0.209	0.004	1.913
II	200	0.393	25	-0.718	0.283	0.015	5.300
III	200	0.393	35	-0.436	0.317	0.016	5.047
IV	200	0.393	45	-0.154	0.340	0.013	3.823
Block 3: Density vs. nozzle temperature and flow rate							
I	154	-1.0	86	1.000	1.065	0.057	5.352
II	176	-0.333	60	0.267	0.651	0.027	4.147
III	198	0.333	32	-0.521	0.332	0.005	1.506
IV	220	1.0	16	-0.971	0.206	0.008	3.883

weight impact tester machine was utilized and the samples were tested in both orientations, i.e., the striker hitting the maximum and the minimum density side of the FGFs.

2.4. Overall methodology of FGF design and manufacturing

Fig. 3 shows the overall workflow for the establishment of MEX AM process to manufacture FGFs. Foamable filament in its unexpanded state was used for the in-situ foam 3D printing process by keeping the nozzle temperatures of the printer higher than the activation temperature, T_{start} of the TEM particles. First, the effects of the print process factors on the density of the printed foams were studied. Nozzle temperature and flow rate were identified as the most influential process factors. Density-process correlation was then identified by density measurements on the samples printed at various conditions. Nozzle temperature and flow rate were both varied individually and simultaneously, and a multiple linear regression analysis was conducted to obtain a statistical model that correlates the density with the temperature, flow rate, and their interaction. The predictability of the regression model was then assessed by comparing the model prediction and experimentally measured densities at several arbitrarily selected process conditions to validate the model.

3. Results and discussion

3.1. Density-process correlations

To establish the correlations between density and process factors, samples with 4 sections (I to IV) were printed. Table 2 shows all the examined nozzle temperature (NT) and flow rate (FR) combinations along with their coded values generated to be used in Minitab software for multiple linear regression analysis. The coded values are the linear transformations of the actual values to a domain of [− 1,+ 1], such that the minimum and maximum actual values of each predictor (factor) correspond to − 1 and + 1, respectively. The use of coded values is essential in the regression analysis with more than one predictor to assure the orthogonality of the design. In other words, once coded, the collinearity between the predictors of NT,FR, and NT×FR (interaction between NT and FR) is eliminated, which facilitates the proper assessment of each predictor effect on the response. Table 2 also gives the density values of each segment of a foam at fixed print parameters. The correlations between the process and the resultant part density and cellular morphology were examined in three steps, represented as blocks 1–3 in Table 2. Block 1 represents the nozzle temperature as the only process variable in the range of 185–215 °C (at a constant flow rate of 35 %) and the obtained density range was 0.126 g cm^{-3}. Block 2 represents the flow rate as the only process variable in the range of 15–45 % (at a constant nozzle temperature of 200 °C) and the obtained density range was 0.131 g.cm^{-3}. Block 1 and 2 were first conducted to correlate the density to each of these factors individually. It is noted that the density range in Block 1 and 2 is relatively small. Block 3 represents the concurrent variation in the nozzle temperature (154–220 °C) and the flow rate (86–16 %) which could produce a density range as large as 0.859 g. cm^{-3}, which was significantly larger than the density range obtained in Block 1 and 2. The NT and FR values in Block 3 were estimated based on their proportional and inverse proportional relations, respectively, with the density such that the combination of the smallest NT and largest FR provides the highest density and the combination of the largest NT and smallest FR provide the smallest density. The extreme values of NT and FR in block 3 were dictated by the printability and dimensional stability of the foams. All the runs given in Table 2 were then used to build the regression model, as further explained later in Section 3.1.2.

3.1.1. Microstructure and cellular morphology

Prior to the statistical analysis of the density as a function of print process parameters, the cellular morphologies and bulk densities obtained in each Block of Table 2 were investigated to better understand the process, microstructure, density relationships. Fig. 4 shows the SEM micrographs of the cross-section of a FGF with sections I, II, III and IV which were printed at the nozzle temperatures of 185, 195, 205 and 215 °C, respectively, as indicated in Block 1 of Table 2. All four sections indicate very uniform and homogeneous cellular morphologies. Fig. 5(a) shows the measured cell size and cell density as a function of nozzle temperature. As seen in Fig. 4, in section I, at nozzle temperature of 185 °C, inter-bead gaps were formed indicating insufficient temperature causing lower degree of TEM expansion, and hence, the cell size was found to be the lowest at 56.8 μm with a cell density of 2.03 × 10^6 cells. cm^{-3} (Fig. 5(a)). In section II, at nozzle temperature of 195 °C, inter-bead gaps faded away (Fig. 4) due to a relatively higher degree of TEM expansion, and both the cell size and cell density increased to 65.6 μm and 2.7 × 10^6 cells.cm^{-3}, respectively. In section IV, at 215 °C, cell size was found to be the highest at 68.02 μm with slight decrease in the cell density to 2.4 × 10^6 cells.cm^{-3}. Higher temperature provided higher degree of expansion resulting in larger cell size [12]. As the temperature increases, the gas pressure inside the TEM microspheres increases while the viscosity of the surrounding polymer matrix decreases, both of which contribute to further enlargement of the TEM micro-balloon. However, no significant difference in cell density was observed from section II-IV indicating that the number of activated TEM particles was similar and probably close to its maximum limit at or around 195 °C.

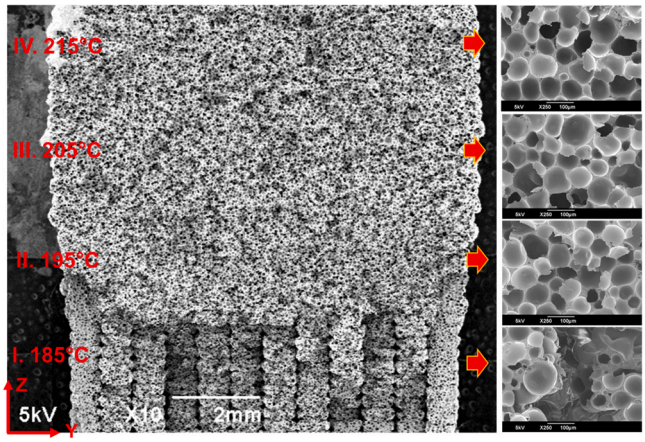

Fig. 4. SEM micrographs showing Y-Z plane cross-section of a printed part with change in the nozzle temperature from 185 to 215 °C at a constant flow rate of 35 %. Left image shows all sections I-IV and their printing temperature conditions from 185–215 °C (Table 2, Block 1). The images on the right show magnified micrographs of each section where the scalebar is 100 μm.

Fig. 6 shows the SEM micrographs of the cross-section of a FGF having four sections each printed at a certain flow rate. Fig. 5(b) also shows the cell size and cell density as a function of the flow rate. In all sections I-IV, at flow rates of 15 %, 25 %, 35 % and 45 %, uniform and homogenous cellular morphologies are observed with no major anomalies. In section I, at flow rate of 15 %, cryo-fractured surface is irregular indicating soft texture of the foam due to very high degree of TEM expansion and the lack of sufficient material throughput. A higher degree of TEM expansion is expected due to longer residence times provided by the lowest flow rate value of 15 %. Longer residence time provides longer time for the heat transfer from the hot end to the polymer melt and thus the available heat and energy to activate the TEM micro-balloons increases, resulting in their further expansion. Cell size was found to be the highest at 85.4 μm with the lowest cell density of 1.08 × 10^6 cells.cm^{-3} (Fig. 5(b)), due to smaller material throughput. Overall, with an increase in the flow rate, the volumetric throughput of the material increased, and the residence time decreased, which caused a consistent increase in the cell density and reduction in the cell size,

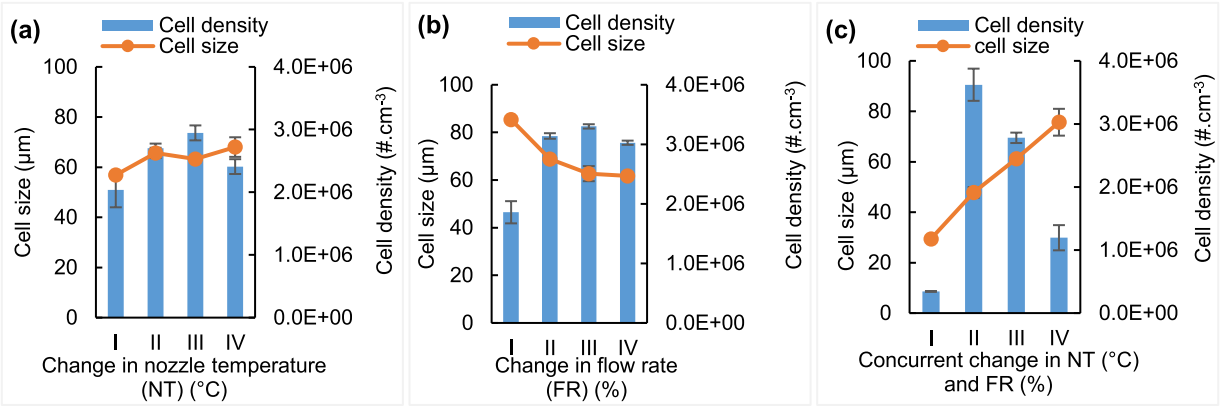

Fig. 5. Cell size and cell density of sections I-IV of the FGFs printed as a function of (a) nozzle temperature, (b) flow rate, and (c) concurrent change in nozzle temperature and flow rate. Sections I-IV in (a), (b) and (c) refer to the same sections in Figs. 4, 6 and 7, respectively.

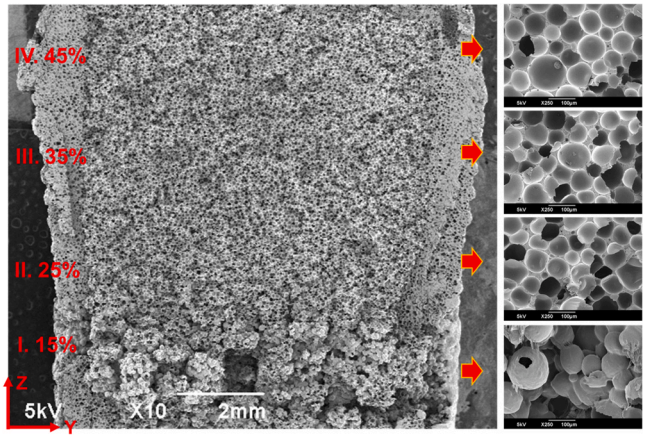

Fig. 6. SEM micrographs showing Y-Z plane cross-section of a printed part with change in the flow rate from 15 to 45 % at a constant nozzle temperature of 200 °C. Image on left at magnification of 10 shows all sections I-IV and their flow rate conditions from 15–45 % (Table 2, Block 2). The images on the right show magnified micrographs of each section where the scalebar is 100 μm.

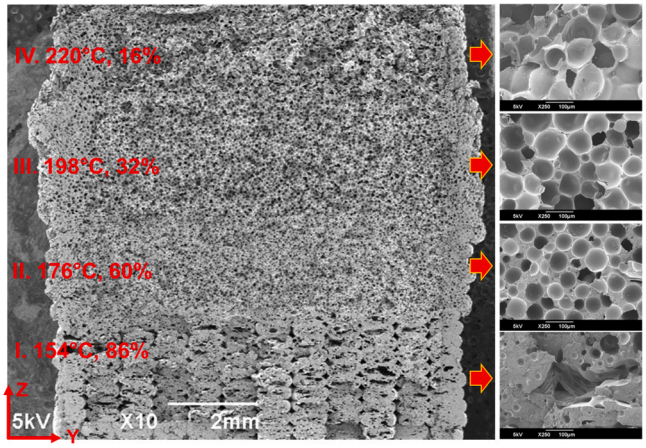

Fig. 7. SEM micrographs showing Y-Z plane cross-section of a printed part with concurrent change in the nozzle temperature and the flow rate from 154 to 220 °C and 86 to 16 %, respectively (Table 2, Block 3). The left image shows all sections I-IV and their nozzle temperature and flow rate conditions. The images on the right show magnified micrographs of each section where the scalebar is 100 μm.

respectively.

After obtaining the density ranges from variable nozzle temperature and flow rate conditions (one factor at a time), additional flow rate and nozzle temperature combinations were examined with a goal of obtaining the widest possible density range. Fig. 7 shows the SEM micrographs of a FGF having four sections printed with the concurrent variation of nozzle temperature and flow rate, which resulted in density values between 0.206 to 1.065 g.cm^{-3} (Block 3 in Table 2). Fig. 5(c) represents the cell size and cell density of each section corresponding to Fig. 7. As seen in Fig. 7, in section I, at nozzle temperature of 154 °C and flow rate of 86 %, inter-bead gaps are formed indicating a very low degree of TEM expansion. A lower degree of TEM expansion is expected due to lower nozzle temperature and shorter residence time provided by the highest flow rate value of 86 %. Both cell size and cell density were found to be the lowest at 29.4 μm and 0.34 × 10^6 cells.cm^{-3} as seen in Fig. 5(c). In remaining sections II-IV no abnormalities are seen with very uniform and homogenous cellular morphologies. In section II, with increase in nozzle temperature to 176 °C and decrease in flow rate to 60 %, the cell size was found to increase to 47.8 μm with an increase in the cell density to 3.62 × 10^6 cells.cm^{-3}. In section III, at nozzle temperature of 198 °C and flow rate of 32 %, cell size further increased to 61.1 μm with decrease in cell density to 2.77 × 10^6 cells.cm^{-3}. And in section IV, at nozzle temperature of 220 °C and flow rate of 16 %, cell size was found to further increase to 75.6 μm with a decrease in cell density to 1.19 × 10^6 cells.cm^{-3}. At section I and II, the nozzle temperature shows a dominant effect as activation of TEM particles increases causing increase in the cell density value, whereas, in section III and IV, due to a decrease in the flow rate, the throughput of the extrudate decreased causing a drop in the cell density. However, from section I to IV, a continuous increase in the cell size (as shown in Fig. 5(c)) is related to a decrease in flow rate which provided increase in the residence time of TEM particles resulting in higher degree of expansion.

3.1.2. *Density-process correlation modeling and validation*

The data of Table 2 was used in constructing a multiple linear regression model in Minitab statistical analysis software. The density was selected as the dependent variable, and the nozzle temperature (NT) and flow rate (FR) were independent variables. The multiple linear regression equation of density vs. nozzle temperature, flow rate, and their interaction is given below:

$$\text{Density} = 0.4793 - 0.2175 \times (C - NT) + 0.2279 \times (C - FR) - 0.1651 \times (C - NT \times FR) \quad (2)$$

where C-FR, C-NT, and C-NT × FR denote the coded values of the flow rate, nozzle temperature, and the interaction of nozzle temperature and flow rate, respectively. Coded values were used instead of the actual values to decrease the correlations between the independent factors.

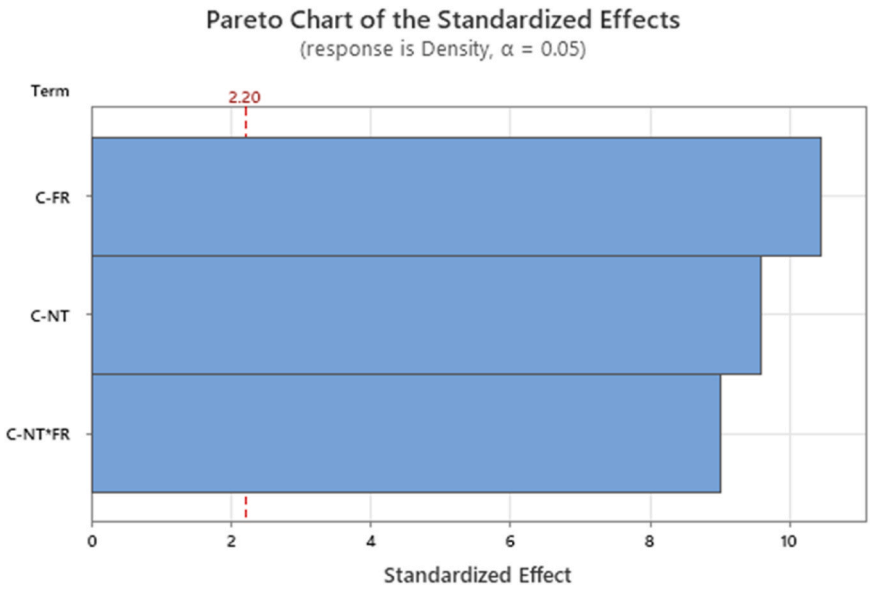

Fig. 8. Pareto chart for multiple linear regression analysis from the data shown in Table 2. Density is the response and C-NT, C-FR and C-NT × FR are continuous predictors.

Table 3
Arbitrarily selected density, ρ_{model} values, their corresponding NT and FR values generated from the regression model, and experimentally measured density values, $\rho_{exp.}$ of the printed parts with their standard deviation (SD) and coefficient of variation (COV). Error is the difference between $(\rho_{exp.} - \rho_{model}) \times 100/\rho_{exp}$.

	ρ_{model} (g cm^{-3})	NT (°C)	FR (%)	Mean $\rho_{exp.}$ (g cm^{-3})	SD $\rho_{exp.}$ (g cm^{-3})	COV $\rho_{exp.}$ (%)	Error (%)
1	0.360	192.3	35.2	0.394	0.019	4.82	8.63
2	0.640	173.2	58.9	0.678	0.038	5.60	5.60
3	0.920	165.5	82.6	0.993	0.06	6.04	7.35

Fig. 8 plots the Pareto chart for the multiple linear regression analysis showing that all the three continuous predictors, i.e., C-FR, C-NT and C-NT × FR are statistically significant, as they all exceed the standardized effect of 2.20, corresponding for a significance level of 5 %. Analysis of variance (ANOVA) also showed that the *P*-value of all the variables in the model is below 2.1×10^{-6} and the smallest *F*-value was 81.25 confirming the significance of all three variables. The coefficient of determination of the model, R^2 was 99.45 % and $R^2_{predicted}$ was 98.25 %. High R^2 values of the model indicate the model capability in predicting the density for new observations.

To assess the prediction capability of the model, three densities were arbitrarily selected and used as input to Eq. (2) to predict the required nozzle temperature and flow rate (Table 3). For a given density, there are two unknown process parameters, i.e., NT and FR. In other words, there are several combinations of NT and FR that could theoretically result in the same density. In order to have an informed estimation of one of the factors, FR was first assumed to follow a simple linear relation with the density based on all the data of Table 2. It should be noted that this is just an estimation and does not have to be exact. The estimated FR value was then used in Eq. (2) to calculate the required nozzle temperature for the desired density. The generated flow rate and nozzle temperature values were then used in the Ideamaker slicing software and the samples were printed and tested for density. Table 3 lists the model density, experimentally measured density, and the differences between the two (error). The maximum error was 8.63 %. Considering that the coefficient of variation (COV) for the experimental replications (Table 3) ranges from 4.82 to 6.04 %, a maximum 8.63 % error for the model prediction is considered very good.

3.2. Part design

The next step before printing the foams was to come up with a part design strategy. FGFs were considered to have distinct sections with different densities but the same thickness. Total height *H* of quasi-static compression samples was 24 mm whereas that was 12 mm for the impact samples. Quasi-static compression samples were discretized into five sections with section thickness, *h* of 4.8 mm ($h = H$/number of section). The impact samples were also discretized into eight sections with section thickness, *h* of 1.5 mm. Koohbor et. al. [28] previously studied the design optimization in discretely graded polyurethane foams where they used a power law function according to the formalism below:

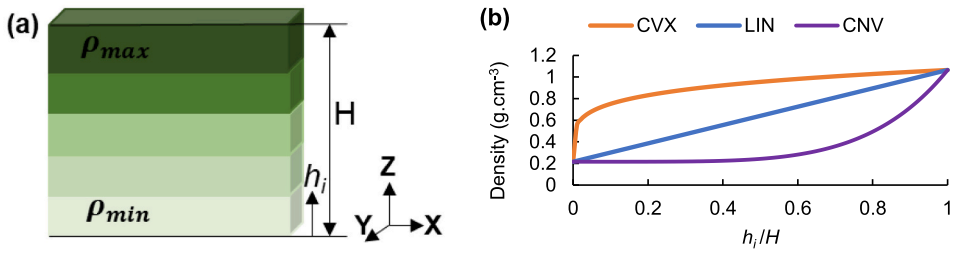

Fig. 9. (a) A schematic of a FGF showing minimum density (ρ_{min}), maximum density (ρ_{max}), section height (h_i) and total height (H) along Z direction, and (b) density vs. normalized height h_i/H showing three different density gradation profiles, i.e., convex (CVX, m=0.2), linear (LIN, m=1), and Concave (CNV, m=5).

Table 4
3D printed quasi-static compression samples with sections I-V of FGFs using three density gradient profiles, i.e., CVX (m= 0.2), LIN (m=1.0) and CNV (m=5.0). In each density gradient profile, the density of each section was calculated following the procedure in Section 3.2 and their corresponding flow rate and nozzle temperature were obtained following the procedure in Section 3.1.

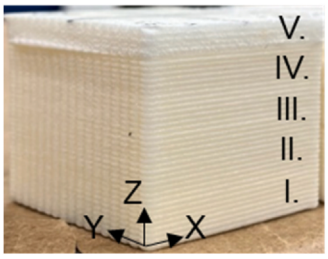

	CVX (m=0.2)		
Section	ρ(h)	Flow rate	Temperature
I.	0.216	23.3	219.2
II.	0.859	77.2	166.8
III.	0.955	85.2	164.9
IV.	1.017	90.3	163.9
V.	1.065	94.4	163.2
ρ_a	0.923	82.5	165.5

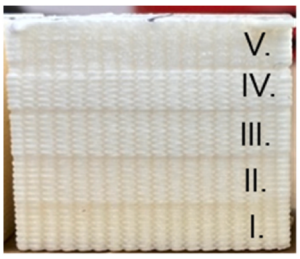

	LIN (m=1)		
Section	ρ(h)	Flow rate	Temperature
I.	0.216	23.3	219.2
II.	0.428	41.1	185.2
III.	0.640	58.8	173.1
IV.	0.852	76.5	167
V.	1.065	94.4	163.2
ρ_a	0.640	58.8	173.1

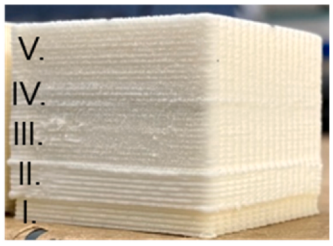

	CNV (m=5)		
Section	ρ(h)	Flow Rate	Temperature
I.	0.216	23.3	219.2
II.	0.217	23.4	218.9
III.	0.242	25.5	211.9
IV.	0.417	40.2	186.2
V.	1.065	94.4	163.2
ρ_a	0.357	35.2	192.3

$$\rho(h_i) = \rho_{\min} + \Delta\rho \left(\frac{h_i}{H}\right)^m \quad (3)$$

$$\rho_a = \frac{1}{H}\sum_{i=1}^{n} \rho_i . h_i \quad (4)$$

$$H = \sum_{i=1}^{n} h_i \quad (5)$$

$$\Delta\rho = \rho_{\max} - \rho_{\min}, 0 \le h_i \le H \quad (6)$$

Eq. (3) shows the density gradient function, $\rho(h_i)$ where $\rho_{\min}$ is the minimum density, $\Delta\rho$is the density range, h_i is the height at section i, H is the total height and m is the gradient exponent. The rate of change of density, i.e., gradient nature depends on the selected exponent, m. Eq. (4) denotes the overall apparent density of the FGF where ρ_i and h_i are the density and the thickness of section i in the part. Eq. (5) denotes the summation of the thicknesses of all sections. Eq. (6) denotes the density range calculated from the maximum ($\rho_{\max}$)and minimum density ($\rho_{\min}$) obtained along the total height H of the FGF. Fig. 9(a) shows a schematic with discretized gradation and Fig. 9(b) shows a graph of three different gradations profiles, i.e., convex (CVX), linear (LIN) and concave (CNV) with exponents values of m= 0.2, m= 1 and m= 5, respectively.

3.3. 3D printing of functionally graded foams (FGFs)

Table 4 shows the printed quasi-static compression samples with three density gradient profiles of CVX (m= 0.2), LIN (m=1) and CNV (m=5). Each profile shows the corresponding flow rate and nozzle temperature values to the densities of each section. As explained in Section 3.2, part design was segmented into five sections and the print process parameters i.e., flow rates and nozzle temperatures generated from the regression models (Section 3.1.2) were input to the slicing software. Using Eq. (3), the density at each section of the FGFs was determined and used in the regression model (Eq. (2)) to generate the corresponding flow rate and nozzle temperature values. For each density profile, a single density foam (SDF) having a density equivalent to the apparent density of the FGF (ρ_a, Eq. (4)) was also printed as a baseline for the mechanical performance assessment. All the FGFs and SDFs were successfully printed with good printability and dimension accuracy and used for mechanical testing in the next section. It is seen that moving from one section to another in each foam sample, the dimensional

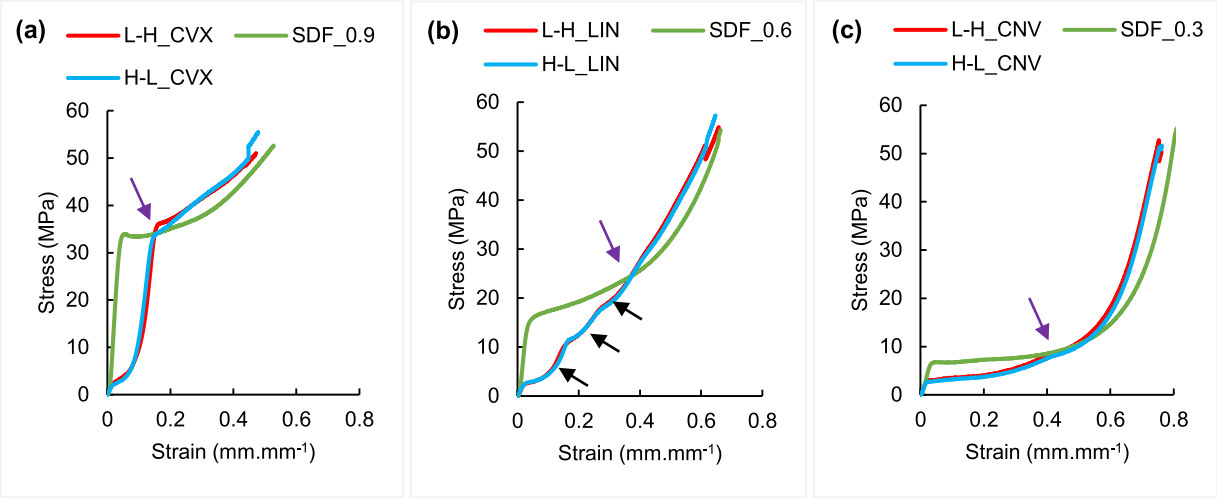

Fig. 10. Representative compressive stress-strain graphs of discretely graded a) CVX, b) LIN, and c) CNV FGFs and their SDF counterparts. SDF_0.9, SDF_0.6 and SDF_0.3 denote SDFs with densities of 0.9, 0.6, and 0.3 g.cm^{-3}, respectively. L-H and H-L denote low to high (i.e., increasing) and high to low (i.e., decreasing) density gradient with respect to the applied load direction. Purple arrows indicate the strain cross over point between FGFs and SDFs. Black arrows in (b) indicate the shoulder observed for LIN FGFs.

accuracy of the foam was maintained reasonably well, unlike the fact that the degree of foam expansion changed from one section to another. This was realized primarily due to the proper combination of NT and FR. As seen in Table 4, the higher NT values were always associated with lower NT values and vice versa. Higher temperatures provided further activation of TEMs towards lower densities, while the lower flow rates reduced the melt mass throughput at the nozzle exit, providing additional space for the foam to expand and shape the raster.

3.4. Mechanical behavior of FGFs

The effects of CVX, LIN and CNV density gradient profiles in FGFs were characterized under both quasi-static compression and low-velocity drop impact loading conditions. The effect of the density profile orientation with respect to the loading direction on the mechanical behavior was also evaluated using LIN FGFs under both compression and impact loading conditions.

3.4.1. Quasi-static compression testing

Fig. 10 depicts the representative quasi-static compressive stress-strain graphs of CVX, LIN, and CNV FGFs along with their SDFs having densities equal to that of the overall apparent density of their FGF counterparts. Comparing the two types of foams in each density gradient profile, it is seen that the graded foams exhibit a more gradual rise of stress, compared to that with the SDFs. Moreover, the cross-over strain (shown with purple color arrow) between the two foam types increases as the density decreases from 0.9 g.cm^{-3} (Fig. 10(a)) to 0.3 g.cm^{-3} (Fig. 10(c)). This indicates that lower stress levels are expected within larger deformations in the graded foams at lower densities. The strain at a given stress value, e.g., 50 MPa were found to increase from CVX to LIN to CNV FGFs. A similar pattern was also observed for SDFs from SDF_0.9 to SDF_0.6 to SDF_0.3. These trends can be related to the overall density of the part. As the overall density is decreased through a change in the cell size and/or cell density, the part becomes more compliant and experiences more deformation under a given external stress level. The plateau region of the stress-strain curve also becomes more extended as the overall density decreases. Based on the density values of block 3 in Table 2 and cell size and cell density values of Fig. 5 (c), it can be concluded that by concurrent change of NT and FR, the desired density of each section can be obtained through changes in both cell size and cell density. It however appears that the cell size has more dominant effect since there is a monotonic relation between the density

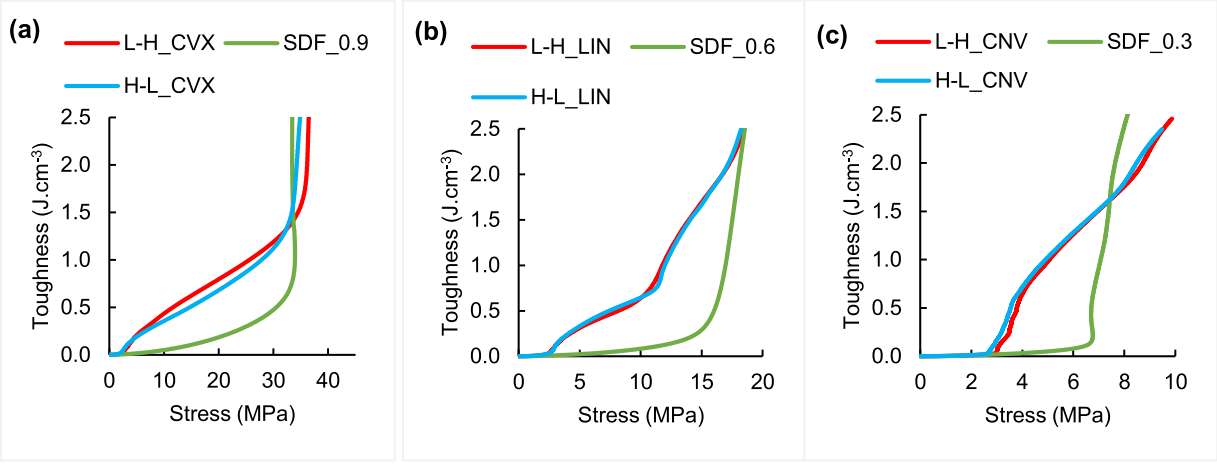

Fig. 11. Representative toughness vs. stress graphs of (a) CVX, (b) LIN, and (c) CNV FGFs and their SDF counterparts. L-H and H-L denote low to high density and high to low density gradient with respect to the applied load direction.

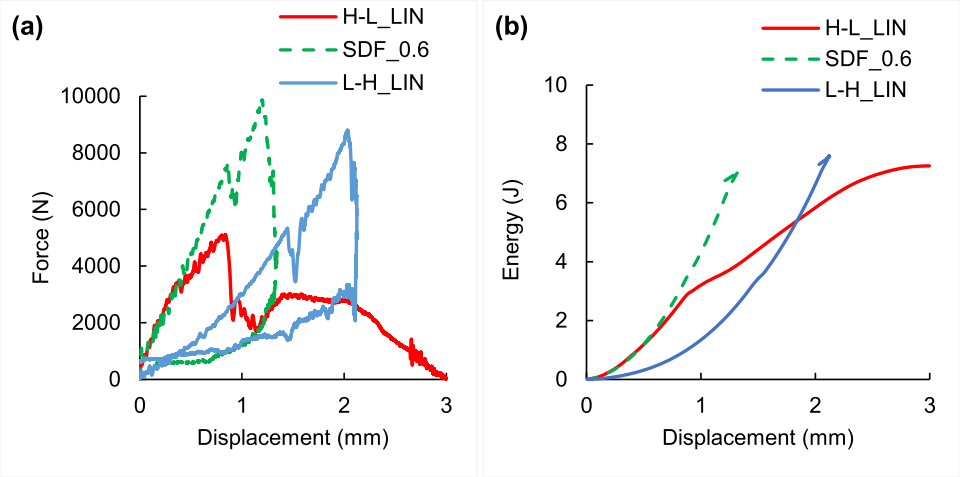

Fig. 12. Representative (a) Force vs. Displacement and (b) Energy vs. Displacement graphs of LIN FGFs with loading in the directions of high-low (H-L_LIN) and low-high (L-H_LIN) density gradients along with their SDF counterpart (SDF_0.6).

and the cell size, while the cell density is maximized at a mediocre density level.

Furthermore, the LIN FGFs showed a stepwise increment of stress vs. strain (marked with black color arrows in Fig. 10(b)). Each shoulder in the stress-strain curve is attributed to a stress level at which an individual section reaches its elastic limit and yields. Such behavior has been previously reported in the literature as well [28,40]. This suggests that by tailoring the density and thickness of each section, desired compressive responses can be achieved in discrete FGFs. The fact that such shoulders are not observed in the CVX and CNV FGFs could be related to the nonlinear change of the density across the thickness such that several sections have relatively close density values and thus they do not produce detectable differences in their stress-strain responses.

In Fig. 10(a-c), L-H (red curves) and H-L (blue curves) represent high to low (H-L) and low to high (L-H) density gradient with respect to the applied load direction. In other words, in L-H case, the lowest density section is at the top and becomes in contact with the moving platen of the machine and the case is vice versa for H-L. The results showed that both L-H and H-L curves overlapped in all the density gradient profiles indicating that there was no significant effect of the density orientation when the samples were loaded under a quasi-static compression force.

Fig. 11 shows the toughness vs. stress graphs for all the three gradient profiles along with their SDF counterparts. In terms of the energy absorption capability, the FGFs greatly outperformed their SDF counterparts at low stress levels before the cross over points. As shown in Fig. 11(a), at a stress level of 30 MPa, the toughness of CVX FGFs was 1.1 J cm^{-3} as opposed to 0.47 J cm^{-3} of its SDF_0.9 counterpart, denoting 130 % improvement in the toughness. At a stress level of 15 MPa, LIN FGFs (Fig. 11(b)) showed a toughness of 1.7 J cm^{-3} and its SDF_0.6 counterparts had a toughness of 0.28 J cm^{-3}, denoting 507 % increase in the toughness. At a stress level of 5 MPa, the CNV FGF (Fig. 11(c)) had toughness of ~1.0 J cm^{-3} whereas its SDF_0.3 counterpart showed a toughness of only 0.05 J cm^{-3} denoting 1900 % increase in the toughness.

However, as the stress increases, at some point, the toughness of SDFs exceeds that of their FGF counterpart. The toughness behavior of FGFs is different from typical SDFs in that the toughness starts building up and increase gradually as the stress level rises, as opposed to the SDF case where the toughness remains relatively low at low stress levels and increases suddenly when it reaches to the beginning of the plateau zone in the stress-strain curve. This initial rapid rise of toughness in FGFs can be leveraged in part design for low stress applications.

3.4.2. *Low-velocity impact testing*

Fig. 12(a) and (b) show the force vs. displacement and energy vs. displacement graphs, respectively, of the LIN FGF tested in high to low (H-L_LIN) and low to high (L-H_LIN density gradient directions. As shown in Fig. 12(a), at the initial linear elastic region, higher slopes were observed in H-L_LIN FGFs, while L-H_LIN FGFs exhibited lower slopes. SDF_0.6 had slopes closer to H-L_LIN FGFs. It appears that the density of the top section of the foams, which comes into contact with the striker first has a dominant effect on the initial slope, and the higher its density, the stiffer is the initial response. It is also noted that H-L_LIN exhibited significantly lower peak force, compared to L-H_LIN, but the force peaked multiple times. Similar effects of density gradient *w.r.t* the loading direction have also been previously reported for aluminum foams under dynamic impact loading [40]. Lower peak forces at the same density and absorbed energy levels are preferred as the stress levels and the transferred load levels can be lower too.

Moreover, the closed curves in force vs. displacement graphs of L-H_LIN FGF and SDF_0.6 (Fig. 12(a)) denote an elastic impact behavior of these foams during testing [41], while H-L_LIN FGF continued the deformation (without any change in the displacement direction) and registered the largest deformation. This difference between the two can be attributed to the density of the parts' lower sections, where H-L_LIN FGF had the lowest density at the lower sections and exhibited the lowest resistance and continued the deformation towards the end of the impact event. While the other two foams had higher densities at the lower sections and exhibited more elastic resistance. The total displacement was also observed to be larger in both H-L_LIN and L-H_LIN FGFs as compared to SDF_0.6.

As seen in Fig. 12(b), irrespective of the gradient and the loading direction, the total energy absorbed at the end of the impact event was similar for all the cases at around 7.0 J. The rate of the energy absorption with displacement was however different for different foams. In SDF_0.6, the energy almost monotonously increased and maxed out at a displacement of around 1.3 mm. H-L_LIN initially behaved similar to SDF_0.6, but at around a displacement of 1 mm, the slope changed, and the energy increased more slowly and lasted until a displacement of about 2.4 mm. L-H_LIN exhibited a more concave up trend with displacement, indicating an increase in the energy rate with displacement as the displacement was increased.

Overall, these results indicate a significant effect of the gradient direction on the peak forces and displacements of LIN FGFs while all having the same energy absorption level. This provides an opportunity to design parts that can absorb similar energy levels but maintain the peak forces at significantly lower levels.

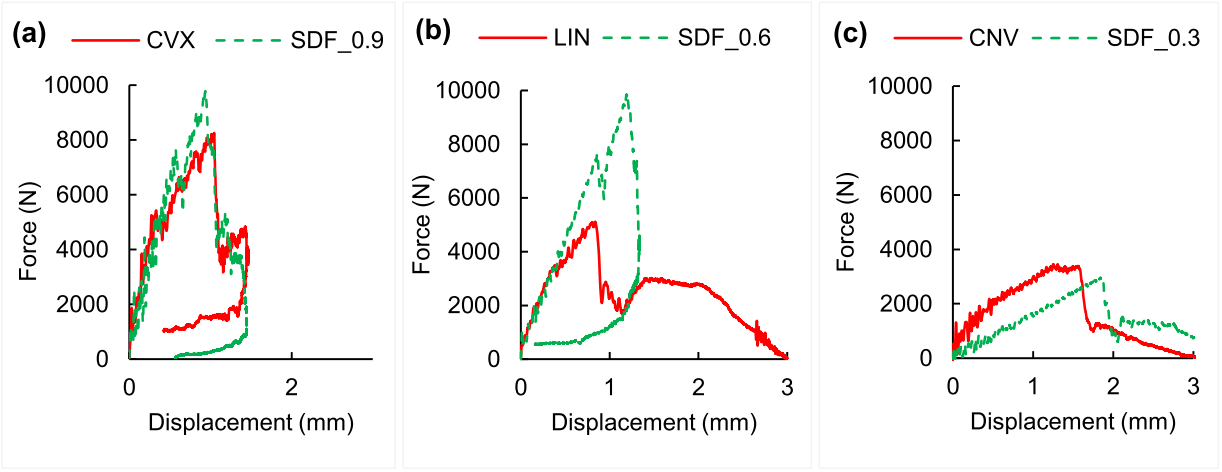

Fig. 13. Representative force vs. displacement graphs of (a) CVX, (b) LIN, and (c) CNV FGFs and their SDF counterparts. All FGFs are tested in high to low (H-L) density gradient with respect to the applied force direction.

Fig. 13 (a–c) shows the force vs. displacement graphs of CVX, LIN, and CNV FGFs along with their SDF counterparts. Comparing CVX, LIN, and CNV FGFs, the peak forces and the initial slopes of force vs. displacement curves showed the order of CVX > LIN > CNV. The higher peak forces and the greater slopes in CVX FGFs are due to its relatively higher stiffness because of having larger number of higher density sections, which is also evident from its higher apparent density of 0.923 g. cm^{-3}. As seen in Fig. 13 (a-b), the CVX and LIN FGFs exhibited lower peak forces, compared to their SDF counterparts having the same density, while having initial slopes similar to those of their corresponding SDF counterparts. The CNV FGFs, however, showed slightly higher slopes and similar peak forces as compared to their SDF_0.3 counterparts. Higher slope and no significant reduction in the peak force of CNV FGF samples can be related to the nature of the concave density gradient design where the top section had a significantly higher density, compared to the apparent density as in the SDF_0.3 part (Table 4). This is likely to impart higher stiffness as well as higher peak forces.

The closed curves in force vs. displacement graphs of CVX FGFs, SDF_0.9 and SDF_0.6 (Fig. 13(a-b)) denotes elastic impact behavior [41], associated with higher density sections, whereas, in LIN FGFs, CNV FGFs and SDF_0.3 (Fig. 13(b-c)), after the peak force, no such closed-curve behavior was observed. This indicates a clear through penetration of the striker and the continuation of the sample deformation in an inelastic manner. This observation together with the larger compliance in the force vs. displacement graphs of CNV FGF, LIN FGF, and SDF_0.3 denotes their relatively ductile behavior, which is a characteristic of the samples or sections of the samples with lower density. Larger compliance in CNV FGFs can be related to a greater number of sections with lower density in the graded profile. Lower density is achieved due to the existence of a more pronounced cellular structure with higher cell density which imparts more ductile behavior [12].

4. Conclusions

In this study, the fabrication of functionally graded structures via in-situ foaming within MEX AM process is reported. Using single screw extruder, foamable feedstock filament was fabricated at a TEM loading of 8.0 wt% and it was utilized as feedstock for 3D printing process. Nozzle temperature and flow rate were considered as the key print process parameters and their impact on the evolved cellular morphologies and resultant bulk densities were investigated. With concurrent change in the nozzle temperature and flow rate, density gradients in the range 0.86 g.cm^{-3} were achieved within a single print. Using statistical analysis, a density-process correlation model was proposed and verified, which was used to obtain the nozzle temperature and flow rate parameters for any desired density value. FGFs were printed with three different density gradient profiles of convex (CVX), linear (LIN) and concave (CNV) and showed very good printability and acceptable dimensional tolerances. Under quasi-static compression testing, CVX FGFs showed higher peak forces with smaller displacements, whereas CNV FGFs showed lower peak forces with larger deformations. In terms of the energy absorption capacity, all FGFs with various gradient profiles outperformed their SDF counterparts at low stress levels. Under low-velocity impact conditions, a significant effect of the density gradient direction *w.r.t.* to the applied load direction was observed. The FGFs impacted from the high-density side exhibited multiple peak behavior with significantly lower peak forces, compared to their SDF equivalents. Overall, this work demonstrated a versatile and facile approach to fabricate FGFs via MEX AM process. FGFs as a single print with tailored density profiles can be used in generative design optimization of AM parts for enhanced mechanical performance and other functionalities.

CRediT authorship contribution statement

Amir Ameli: Writing – review & editing, Validation, Supervision, Resources, Project administration, Methodology, Funding acquisition, Conceptualization. **Karun Kalia:** Writing – original draft, Investigation, Formal analysis, Data curation.

Declaration of Competing Interest

The authors declare the following financial interests/personal relationships which may be considered as potential competing interests: Amir Ameli reports financial support was provided by National Science Foundation.

Data availability

Data will be made available on request.

Acknowledgement

This work was supported by the National Science Foundation under Grant Number 1822147 (Center for Science of Heterogeneous Additive Printing of 3D Materials (SHAP3D)) and the SHAP3D I/UCRC Members. Any opinions, findings, and conclusions or recommendations expressed in this material are those of the author(s) and do not necessarily reflect the views of the national Science Foundation or SHAP3D members. The authors would like to thank NatureWorks LLC and Sekisui Chemical Co. Ltd. for providing the materials.

References

[1] M. Nofar, J. Utz, N. Geis, V. Altstädt, H. Ruckdäschel, Foam 3D printing of thermoplastics: a symbiosis of additive manufacturing and foaming technology, Adv. Sci. 2105701 (2022) 1–18, https://doi.org/10.1002/advs.202105701.

[2] B. Sun, L. Wu, Research progress of 3D printing combined with thermoplastic foaming, Front. Mater. (2022) 1–15, https://doi.org/10.3389/fmats.2022.1083931.

[3] M. Li, J. Jiang, B. Hu, W. Zhai, Fused deposition modeling of hierarchical porous polyetherimide assisted by an in-situ CO_2 foaming technology, Compos. Sci. Technol. 200 (2020), 108454, https://doi.org/10.1016/j.compscitech.2020.108454.

[4] S. Zhang, X. Shi, Z. Miao, H. Zhang, X. Zhao, K. Wang, J. Qin, G. Zhang, 3D printed polyurethane tissue engineering scaffold with hierarchical microcellular foam structure and antibacterial properties, Adv. Eng. Mater. (2022), https://doi.org/10.1002/adem.202101134.

[5] J. Zhang, D. Li, W. Zhu, Y. Li, In situ 3D printing of poly-ether-ether-ketone / poly-ether-imide hierarchical cellular foams containing electromagnetic absorbent, Addit. Manuf. 59 (2022), 103181, https://doi.org/10.1016/j.addma.2022.103181.

[6] P. Song, C. Zhou, H. Fan, B. Zhang, X. Pei, Y. Fan, Q. Jiang, R. Bao, Q. Yang, Z. Dong, X. Zhang, Novel 3D porous biocomposite scaffolds fabricated by fused deposition modeling and gas foaming combined technology, Compos. Part B Eng. 152 (2018) 151–159, https://doi.org/10.1016/j.compositesb.2018.06.029.

[7] B.K. Park, C.-J. Kim, D.E. Kwon, Y.-W. Lee, Design and fabrication of partially foamed grid structure using additive manufacturing and solid state foaming, Processes (2020), https://doi.org/10.3390/pr8121594.

[8] A.R. Damanpack, A. Sousa, M. Bodaghi, Porous PLAs with controllable density by FDM 3D printing and chemical foaming agent, Micromachines 12 (2021) 866, https://doi.org/10.3390/mi12080866.

[9] K. Zarybnicka, P. Lepcio, J. Svatik, J. Jancar, F. Ondreas, Effect of the nanoparticles on the morphology and mechanical performance of thermally blown 3D printed HIPS foams, J. Appl. Polym. Sci. (2022) 1–11, https://doi.org/10.1002/app.53413.

[10] H. Andersson, J. Ortegren, R. Zhang, M. Grauers, H. Olin, Variable low-density polylactic acid and microsphere composite material for additive manufacturing, Addit. Manuf. 40 (2021), https://doi.org/10.1016/j.addma.2021.101925.

[11] J. Wang, H. Xie, Z. Weng, T. Senthil, L. Wu, A novel approach to improve mechanical properties of parts fabricated by fused deposition modeling, Mater. Des. 105 (2016) 152–159, https://doi.org/10.1016/j.matdes.2016.05.078.

[12] K. Kalia, B. Francoeur, A. Amirkhizi, A. Ameli, In situ foam 3D printing of microcellular structures using material extrusion additive manufacturing, ACS Appl. Mater. Interfaces 14 (2022) 22454–22465, https://doi.org/10.1021/acsami.2c03014.

[13] K. Kalia, A. Ameli, Understanding the process-microstructure-property relationships in material extrusion additive manufacturing of polylactic acid microcellular foams, Addit. Manuf. 72 (2023), 103636, https://doi.org/10.1016/j.addma.2023.103636.

[14] A. Yousefi Kanani, A. Kennedy, Effect of the material extrusion process parameters on the compressive properties of additively manufactured foamed and nonfoamed polylactic acid structures, 3D Print. Addit. Manuf. 00 (2022), https://doi.org/10.1089/3dp.2022.0091.

[15] A.Y. Kanani, A.E.W. Rennie, S.Z.Bin AbdRahim, Additively manufactured foamed polylactic acid for lightweight structures, Rapid Prototyp. J. 29 (No. 1) (2022) 50–66, https://doi.org/10.1108/RPJ-03-2022-0100.

[16] M.J. Prajapati, A. Kumar, S.C. Lin, J.Y. Jeng, Multi-material additive manufacturing with lightweight closed-cell foam-filled lattice structures for enhanced mechanical and functional properties, Addit. Manuf. 54 (2022), 102766, https://doi.org/10.1016/j.addma.2022.102766.

[17] M.J. Prajapati, A. Kumar, S.C. Lin, J.Y. Jeng, Closed-cell metamaterial composites 3D printed with hybrid FFF process for tunable mechanical and functional properties, Thin-Walled Struct. 192 (2023), 111168, https://doi.org/10.1016/j.tws.2023.111168.

[18] M.J. Prajapati, A. Kumar, S.C. Lin, J.Y. Jeng, Reducing mechanical anisotropy in material extrusion process using bioinspired architectured lattice structures, Addit. Manuf. 66 (2023), 103480, https://doi.org/10.1016/j.addma.2023.103480.

[19] S. Suethao, D.U. Shah, W. Smitthipong, Recent progress in processing functionally graded polymer foams, Materials 13 (2020) 1–16, https://doi.org/10.3390/ma13184060.

[20] O. Rahman, B. Koohbor, Optimization of energy absorption performance of polymer honeycombs by density gradation, Compos. Part C. Open Access. 3 (2020), 100052, https://doi.org/10.1016/j.jcomc.2020.100052.

[21] K.Z. Uddin, G. Youssef, M. Trkov, H. Seyyedhosseinzadeh, B. Koohbor, Gradient optimization of multi-layered density-graded foam laminates for footwear material design, J. Biomech. 109 (2020), 109950, https://doi.org/10.1016/j.jbiomech.2020.109950.

[22] N. Gupta, E. Woldesenbet, P. Mensah, Compression properties of syntactic foams: effect of cenosphere radius ratio and specimen aspect ratio, Compos. Part A Appl. Sci. Manuf. 35 (2004) 103–111, https://doi.org/10.1016/j.compositesa.2003.08.001.

[23] B. Dileep, R. Prakash, H.S. Bharath, P. Jeyaraj, M. Doddamani, Dynamic behavior of concurrently printed functionally graded closed cell foams, Compos. Struct. 275 (2021), 114449, https://doi.org/10.1016/j.compstruct.2021.114449.

[24] G.S. Dhaliwal, G.M. Newaz, Flexural response of degraded polyurethane foam core sandwich beam with initial crack between facesheet and core, Materials 13 (2020) 1–18, https://doi.org/10.3390/ma13235399.

[25] G. Wang, J. Liu, J. Zhao, S. Li, G. Zhao, C.B. Park, Structure-gradient thermoplastic polyurethane foams with enhanced resilience derived by microcellular foaming, J. Supercrit. Fluids 188 (2022), 105667, https://doi.org/10.1016/j.supflu.2022.105667.

[26] B. Koohbor, S. Ravindran, A. Kidane, In situ deformation characterization of density-graded foams in quasi-static and impact loading conditions, Int. J. Impact Eng. 150 (2021), 103820, https://doi.org/10.1016/j.ijimpeng.2021.103820.

[27] N. Gupta, A functionally graded syntactic foam material for high energy absorption under compression, 61 (2007) 979–982. https://doi.org/10.1016/j.matlet.2006.06.033.

[28] B. Koohbor, A. Kidane, Design optimization of continuously and discretely graded foam materials for efficient energy absorption, Mater. Des. 102 (2016) 151–161, https://doi.org/10.1016/j.matdes.2016.04.031.

[29] C. Zhou, P. Wang, W. Li, Fabrication of functionally graded porous polymer via supercritical CO 2 foaming, Compos. Part B Eng. 42 (2011) 318–325, https://doi.org/10.1016/j.compositesb.2010.11.001.

[30] M. Sauceau, J. Fages, A. Common, C. Nikitine, E. Rodier, New challenges in polymer foaming: a review of extrusion processes assisted by supercritical carbon dioxide, Prog. Polym. Sci. 36 (2011) 749–766, https://doi.org/10.1016/j.progpolymsci.2010.12.004.

[31] J.A.V. Jiménez, N. Le Moigne, J.-C. Bénézet, M. Sauceau, R. Sescousse, J. Fages, Foaming of PLA composites by supercritical fluid-assisted processes: a review, Molecules 25 (2020), https://doi.org/10.3390/molecules25153408.

[32] H. Wu, G. Zhao, G. Wang, W. Zhang, Y. Li, A new core-back foam injection molding method with chemical blowing agents, Mater. Des. 144 (2018) 331–342, https://doi.org/10.1016/j.matdes.2018.02.043.

[33] A. Ameli, M. Nofar, D. Jahani, G. Rizvi, C.B. Park, Development of high void fraction polylactide composite foams using injection molding: crystallization and foaming behaviors, Chem. Eng. J. 262 (2015) 78–87, https://doi.org/10.1016/j.cej.2014.09.087.

[34] D. Jahani, A. Ameli, P.U. Jung, M.R. Barzegari, C.B. Park, H. Naguib, Open-cell cavity-integrated injection-molded acoustic polypropylene foams, Mater. Des. 53 (2014) 20–28, https://doi.org/10.1016/j.matdes.2013.06.063.

[35] S. Ghaffari Mosanenzadeh, H.E. Naguib, C.B. Park, N. Atalla, Design and development of novel bio-based functionally graded foams for enhanced acoustic capabilities, J. Mater. Sci. 50 (2015) 1248–1256, https://doi.org/10.1007/s10853-014-8681-6.

[36] S.R.G. Bates, I.R. Farrow, R.S. Trask, Compressive behaviour of 3D printed thermoplastic polyurethane honeycombs with graded densities, Mater. Des. 162 (2019) 130–142, https://doi.org/10.1016/j.matdes.2018.11.019.

[37] A. Pawar, G. Ausias, Y.-M. Corre, Y. Grohens, J. Férec, Mastering the density of3D printed thermoplastic elastomer foam structures with controlled temperature, Addit. Manuf. 58 (2022), https://doi.org/10.1016/j.addma.2022.103066.

[38] K. Kalia, B. Francoeur, A. Amirkhizi, A. Ameli, Fabrication of expandable filaments towards in-situ foam 3D printing of microcellular poly (lactic acid),SPE ANTEC, 2022.

[39] M. Ozdemir, Z. Doubrovski, Xpandables: Single-filament multi-property 3D printing by programmable foaming, in: Ext. Abstr. 2023 CHI Conf. Hum. Factors Comput. Syst., Association for Computing Machinery, 2023: pp. 1–7. https://doi.org/10.1145/3544549.3585731.

[40] X. Zhang, H. Zhang, Optimal design of functionally graded foam material under impact loading, Int. J. Mech. Sci. 68 (2013) 199–211, https://doi.org/10.1016/j.ijmecsci.2013.01.016.

[41] K.R. Ramakrishnan, K. Shankar, Experimental and numerical analysis of low-velocity impact of plastic laminates, Fatigue Fract. Eng. Mater. Struct. 36 (2013) 1153–1163, https://doi.org/10.1111/ffe.12099.